Low-coherence optical tomography in turbid tissue: theoretical analysis

Yingtian Pan, Reginald Birngruber, Jürgen Rosperich, and Ralf Engelhardt

On the basis of white-light interferometry and statistical optics, a theoretical model for low-coherence optical tomography is presented that establishes the relation of interference modulation with path-length-resolved reflectance and that can provide analytical expressions and numerical solutions by means of a Fourier transform. The Monte Carlo technique is used to simulate the path-length-resolved reflectance from different multilayer tissue phantoms. Theoretical analyses and preliminary experimental results suggest that, unlike time-resolved spectroscopy, low-coherence optical tomography detects the local relative variations of path-length-resolved reflectance from the turbid tissues.

Key words: Low-coherence interferometry, Fourier transform, coherence-gated imaging, path-length-resolved Monte Carlo simulation, tissue-optical properties.

1. Introduction

Noninvasive optical and near-infrared imaging of obscure structures in turbid media, especially in biological tissues, is a difficult and challenging problem in modern optical technology, which has long been hindered by the existence of overwhelming light scattering that severely reduces image contrast and degrades spatial resolution.[1–3] Optical methods are more advantageous than the conventional modalities in that safe doses of optical and near-infrared illumination are used instead of dangerous ionizing x-ray radiation. In recent years, significant progress has been made that may lead to a striking means for *in vivo* optical diagnosis of cancer and some other diseases.[4,5] Patterson *et al.*[6] proposed a theoretical model on the basis of a time-dependent diffusion theory that offers analytical expressions that can be used to derive the scattering and the absorption coefficients of tissue from the measurements of photon-migration transients, i.e., time-resolved reflectance from a semi-infinite, homogeneous medium. Chance *et al.*[7] reported time-resolved spectroscopy for the determination of the brain oxygenation state in which the slopes of decay curves with time from a picosecond-pulsed laser reflect the absorbance change of hemoglobin concentrations. Alfano's and Svan-berg's groups successfully presented time-resolved transillumination imaging through breast tissue by discriminating the least-scattered, ballistic photons.[8,9] Yoon *et al.*[10] reported the determination of absorption and scattering coefficients through the analysis of the coherent backscattered peak. Some other techniques, such as frequency modulation,[11,12] speckle detection,[13] and electronic holography,[14] have also been studied extensively. Recently several time-resolved image reconstruction and optical computer tomography algorithms have been implemented that might find potential applications for clinical diagnosis in the near future.[15–20]

In contrast to time-of-flight measurement, which is made feasible only through the use of expensive and complicated picosecond and femtosecond laser pulses and ultrafast optical detection techniques, the newly established optical low-coherence tomography (OCT) provides an attractive alternative. Low-coherence fiber-optic reflectometry has been used for surface contour mapping and micrometer-scale ranging in the retina.[21–23] This principle has been further extended by Huang *et al.* to three-dimensional tomography by the performance of two-dimensional lateral scans.[24] This technique allows the localization of the reflecting sites within a transparent sample with a spatial resolution of the order of 10-μm, limited primarily by the coherence length of the light source and the beam diameter. With optical heterodyne detection, an extremely high detection sensitivity has been achieved with a higher than 100-dB dynamic range.[25] Although OCT has been successfully applied to map the anterior and the posterior segments

of the eye *in vivo*,[26] only a few measurements have so far been reported for turbid tissue, and nearly no theoretical analysis has been presented because of complications caused by multiple scattering.[27] There are several open questions, such as what can OCT detect in turbid tissue? Is it in principle equivalent to the time-resolved technique? To answer these questions, we focus on analyzing the physical principle of OCT in turbid tissue and, on that basis, evaluate its potential performances in multilayer samples by means of Monte Carlo (MC) simulation and some preliminary experimental results.

2. Theory

As stated above, OCT works on a principle that is similar to ultrasound brightness-mode imaging in that a low-coherence optical reflectometer collects the longitudinal profiles of the light reflected from a sample while a transverse scan provides lateral imaging information for three-dimensional tomoreconstruction.[24] The central part is essentially a Michelson or a Mach–Zehnder interferometer illuminated by a low coherent light source, as depicted in Fig. 1. One arm of the interferometer is replaced by the sample under measurement. The reference mirror is shifted with constant speed v_r to produce interference modulation with Doppler frequency $f_D = 2v_r/\lambda$ for optical heterodyne detection, where λ is the mean wavelength. Then the interference can occur at detector PD only when the path difference between these two waves is less than the coherence length of the light.

The principle of low-coherence optical reflectometry can be analyzed in terms of the theory of two-beam interference for partially coherent light. Assuming that the sample in Fig. 1 is a mirror and that the polarization effects of light are ignored, $E_s(t - L_{s0}/c)$ and $E_r(t - L_r/c)$ are scalar complex functions that present the light fields from the sample and the reference arms of a Michelson interferometer, respectively. L_{s0} and L_r are the corresponding optical path

Fig. 1. Schematic diagram of an optical low-coherence interferometer: SLD, superluminescence diode; PD, photodiode; L_{s0}, L_r, round-trip optical path lengths of sample and reference arms, respectively; n_0, refractive index of air; v_r, line speed of piezoelectric transducer scan.

lengths. Because of time invariance of the light field, the resultant intensity at detector PD is then given by

$$I_d(\tau) = \langle [E_s(t) + E_r(t + \tau)][E_s(t) + E_r(t + \tau)]^* \rangle, \quad (1)$$

where the angular brackets denote a long-time average, i.e.,

$$\langle f(t) \rangle = \lim_{T \to \infty} \frac{1}{2T} \int_{-T}^{T} f(t) \mathrm{d}t.$$

$\tau = \Delta L/c$ is the time delay corresponding to the round-trip optical path-length difference between these two beams, i.e., $\Delta L = L_{s0} - L_r = 2n_0(l_{s0} - l_r)$. $n_0 = 1$ is the refractive index of air, and l_{s0}, and l_r are the geometric lengths of these two arms, as indicated in Fig. 1. Because $I_s = \langle E_s(t)E_s^*(t) \rangle$ and $I_r = \langle E_r(t + \tau)E_r^*(t + \tau) \rangle$, Eq. (1) can then be written as

$$I_d(\tau) = I_s + I_r + 2(I_s I_r)^{1/2} \mathrm{Re}[V_{\mathrm{mc}}(\tau)], \quad (2)$$

which is termed the generalized interference law for partially coherent light. $V_{\mathrm{mc}}(\tau)$ is the normalized form of the mutual coherence function, which is defined as

$$V_{\mathrm{mc}}(\tau) \equiv \frac{\langle E_s(t)E_r^*(t + \tau) \rangle}{(I_s I_r)^{1/2}}. \quad (3)$$

For quasi-monochromatic light[28] that satisfies $\Delta\nu \ll \bar{\nu}$ and $\Delta\nu\tau \ll 1$, where $\Delta\nu$ is the optical frequency bandwidth and $\bar{\nu}$ is the mean frequency, the complexity of spectral compositions of the light may be ignored, and the phase difference with respect to the optical path delay can be approximated as $\varphi = 2\pi\bar{\nu}\tau$. Moreover, as the Michelson interferometer is an amplitude-splitting interferometer in which $E_s(t)$ and $E_r(t)$ coalesce from a primarily single wave front $E(t)$, spatial coherence can be neglected and the complex mutual coherence reduces to self-coherence. Consequently Eq. (2) can be derived as

$$I_d(\tau) = I_s + I_r + 2(I_s I_r)^{1/2}|V_{\mathrm{tc}}(\tau)|\cos 2\pi\bar{\nu}\tau. \quad (4)$$

The temporal coherence function $V_{\mathrm{tc}}(\tau)$ can be easily obtained when $E(t)$ is substituted for $E_s(t)$ and $E_r(t)$ in Eq. (3), i.e., $V_{\mathrm{tc}}(\tau) \equiv \langle E(t)E^*(t + \tau) \rangle / I$, where $I = \langle E(t)E^*(t) \rangle$ is the incident irradiance of the light source. For partially coherent light, $|V_{\mathrm{tc}}(\tau)|$, where $0 < |V_{\mathrm{tc}}(\tau)| < 1$, represents a measure of temporal coherence that is related to the coherence time (coherence length) and correspondingly the optical bandwidth of the light source. According to Fourier optics, the self-coherence function $V_{\mathrm{tc}}(\tau)$ is indeed the Fourier transform of the power spectral density of the light source.[29] For a superluminescence diode (SLD), if we assume that the power spectrum has Gaussian line shape, i.e., $p(\lambda) \propto \exp[-4 \ln 2(\lambda - \bar{\lambda})^2/\Delta\lambda^2]$, we find that the output interference intensity also has a

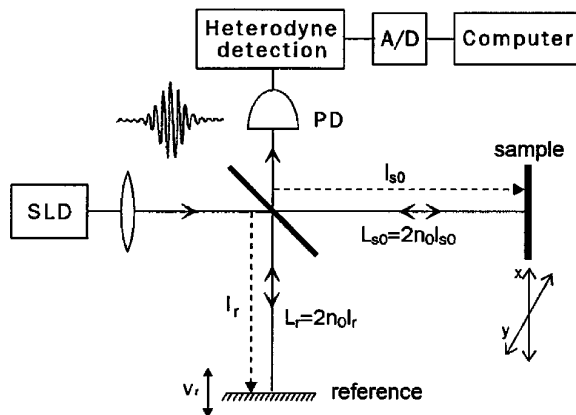Gaussian profile, as shown in Fig. 2. Equation (4) can then be expressed as

$$I_d(\Delta L) = I_s + I_r + 2(I_s I_r)^{1/2} |V_{tc}(\Delta L)| \cos \bar{k} \Delta L, \quad (5)$$

where $\bar{k} = 2\pi/\bar{\lambda}$ is the average wave number and the relation $\bar{\lambda} = c/\bar{\nu}$ is used to transform from time domain into path domain. The interference term is actually a cosine function multiplied by a Gaussian autocorrelation function $|V_{tc}(\Delta L)|$ given by[30]

$$|V(\Delta L)| = \exp[-4(\Delta L/L_c)^2], \quad (6)$$

where L_c is the coherence length that is related to the full-width-half-maximum (FWHM) bandwidth $\Delta\lambda$ of the light source, namely,

$$L_c = \left(\frac{4\sqrt{\ln 2}}{\pi}\right)\left(\frac{\bar{\lambda}^2}{\Delta\lambda}\right).$$

From Eq. (5) we can see that, if the sample is a translucent medium, the detected interference signal, i.e., the envelope of the measured interferogram, shows just the autocorrelation function of the light that represents its Fourier transform of the spectral distribution. Figure 2 shows the measured power spectrum and the autocorrelation function that can be well fit into Gaussian profiles. The typical value of L_c for a SLD is ~15 µm in free space and 20 µm in tissue, if we assume the group velocity refractive index of tissue to be 1.37. Such a low coherence interferometer can certainly be used to locate the reflective boundaries within a transparent sample, such as the eye, with micrometer-range spatial resolution.[26]

However, in scattering media such as turbid tissue, the problem becomes more complicated. The overwhelming scattering events distort the waveform distribution of the reflected light field. For example, the optical paths of the reflected waves, even those from a mirror immersed in a highly scattering medium, will dissipate into a continuously distributive sequence. In other words, the waveforms in scattering media will be randomized. As a consequence, a relevant model has to be developed that can explain what OCT detects in turbid tissue.

As shown in Fig. 3, light reflected from a random medium can be divided into two categories: least-backscattered light which undergoes only single or very little scattering, and diffusely reflected light, which undergoes tremendous scattering events. In the principle of the classical theory of scattering,[31] least-scattered light still maintains coherence,[10] whereas multiply scattered light will lose coherence. For simplicity in mathematics, in the following deduction we neglect the depolarizing effects of multiple scattering and assume that all the waveforms collected by the detector with path-length difference ΔL falling within the coherence length L_c will interfere. Then, according to Eq. (1), the corresponding optical irradiance at the detector is obtained by the superposition of all the light fields reflected from within the scattering sample and the reference mirror to give

$$I_d(\tau) = \left\langle \left[\int_{L_{s0}}^{\infty} E_s'(t, L_s)dL_s + E_r(t + \tau) \right] \right.$$

$$\left. \times \left[\int_{L_{s0}}^{\infty} E_s'(t, L_s)dL_s + E_r(t + \tau) \right]^* \right\rangle, \quad (7)$$

where $L_s = L_{s0} + L_s'$. L_{s0} is the round-trip path length to the sample surface, as indicated in Fig. 1. $L_s' = \Sigma n_s l_i$ is the total path length within the sample that accumulates each scattering free path l_i as shown in Fig. 3, where n_s is the refractive index of the sample. $E'(t, L_s)$ is defined as the path-length-resolved field density given by $E'(t, L_s) = \partial E(t, L_s)/\partial L_s$. Note that Eq. (7) actually represents the multibeam interferences among different waveforms reflected
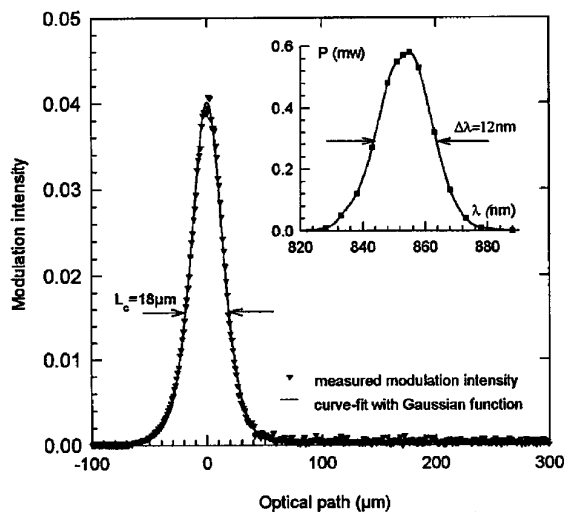

Fig. 2. Measured autocorrelation function and power spectral distribution of a SLD. $\bar{\lambda} \approx 0.85$ µm, $L_c \approx 15$ µm. The solid curve is a least-squares fit of the Gaussian function.
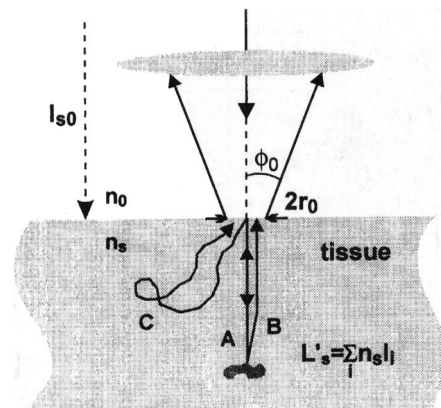

Fig. 3. Schematic that describes light transport and escaping geometry for M-C modeling: A, B, single-scattered and least-backscattered light, respectively; C, multiply scattered light; L_s', l_{s0}, path length within the tissue and round-trip geometric length to the tissue surface (see l_{s0} in Fig. 1). The shaded area represents microstructures.

from the sample and the reference because of multiple scattering. However, the integration term that represents the interference effects among sample waveforms is independent of the reference scan characterized by delay τ. Consequently Eq. (7) can be simplified as

$$I_d(L_r) = I_s + I_r + 2(I_rI_s)^{1/2} \int_{-\infty}^{\infty} [R(L_s)]^{1/2} |V_{tc}(\Delta L)|$$

$$\times \cos \overline{k}\Delta L dL_s, \tag{8}$$

where $R(L_s) = [dI_s(L_s)/dL_s]/I_s$ is the path-length-resolved diffuse reflectance, and I_s is the reflected intensity given by $\langle \int_{L_{s0}}^{\infty} E_s'(t, L_s)dL_s \int_{L_{s0}}^{\infty} E_s'^*(t, L_s)dL_s \rangle$. The integration term in Eq. (8) indicates that the low-coherence interference modulation is equal to the product of mutual correlation of two functions, i.e.,

$$\tilde{I}_d(L_r) = 2(I_sI_r)^{1/2}[[R(L_s)]^{1/2} \otimes C(L_s)], \tag{9}$$

where $\otimes$ denotes the convolution operator. $C(L_s)$, which is defined here as low-coherence function, is equal to $\exp[-4(L_s/L_c)^2]\cos \overline{k}L_s$ if a Gaussian profile is assumed. Then, according to the convolution theorem, it can be expressed in the frequency domain as

$$\tilde{I}_d(L_r) = 2(I_sI_r)^{1/2} \mathscr{F}^{-1}[R_s(k)H(k)], \tag{10}$$

where $\mathscr{F}^{-1}$ denotes an inverse Fourier transform. $R_s(k) = \mathscr{A}[R^{1/2}(L_s)]$ shows the frequency distribution of function $R^{1/2}(L_s)$. From the viewpoint of optical information processing, $H(k)$ can be defined as the optical transfer function (OTF) of the low-coherence interferometry, which is given when the Fourier transform of $C(L_s)$ is evaluated as

$$H(k) = K \exp[-(k - \overline{k})^2(L_c/4)^2], \tag{11}$$

where K is a constant and $\overline{k} = 2\pi/\overline{\lambda}$. As demonstrated in Fig. 4, $H(k)$ is actually a narrow bandpass filter centered at the high-frequency range of $\overline{k} \approx 7.9$ μm^{-1} with a (FWHM) bandwidth of $\Delta k = 4 \ln 2$ $L_c \approx 0.2$ μm^{-1} if we assume that $\overline{\lambda} \approx 0.8$ μm and $L_c \approx 18$ μm. Only the overlapped frequency range of $R_i(k)$ and $H(k)$ indicated by the shaded area contributes to the low-coherence modulation according to Eq. (10). This implies that, unlike the time-resolved technique that acts as an optical low-pass filter of bandwidth $B \propto 1/\Delta\tau$ that collects directly the diffuse reflectance within the time interval, depending on its temporal resolution $\Delta\tau$, OCT correlates to only the fast-varying components, i.e., the high-order derivative of $R^{1/2}(L_s)$ with $\Delta L_s \approx 2\pi/\overline{k} = \overline{\lambda}$.

In order to give a quantitative explanation, Fig. 5(b) shows an example of an actual calculation of the interference modulation versus path length from known $R^{1/2}(L_s)$ by Eq. (8). For simplicity in Fourier transform, $R^{1/2}(L_s)$ is assumed to be a Gaussian function plus another relatively small Gaussian lo-
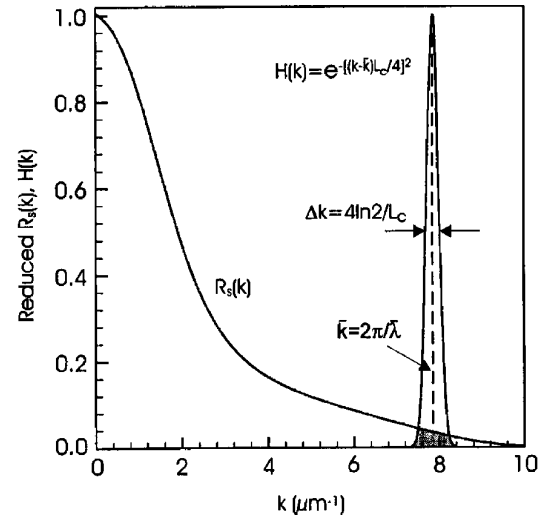

Fig. 4. OCT transfer function $H(k)$ and reflectance distribution $R_s(k)$ in the frequency domain: $L_c = 18$ μm, $\overline{\lambda} = 0.8$ μm, $\overline{k} = 2\pi/\overline{\lambda} \approx 7.9$ μm^{-1}, $\Delta k = 4 \ln 2/L_c \approx 0.2$ μm^{-1}.

cated at $L_s = 500$ μm [see legend in Fig. 5(a)]. Figure 5(b) is similar to the typical $R^{1/2}(L_s)$ distribution in scattering tissue, and Fig. 5(a) simulates a perturbance induced by the local variation of tissue-optical properties. The resultant interference modulation at $L_s = 500$ μm corresponding to this slight perturbance can be approximately derived as

$$\tilde{I}_d(L_r) \propto \exp(-4\overline{k}^2L_0^2)\exp[-4(L_r - 500)^2/L_c^2]$$

$$\times \cos[\overline{k}(L_r - 500)], \tag{12}$$

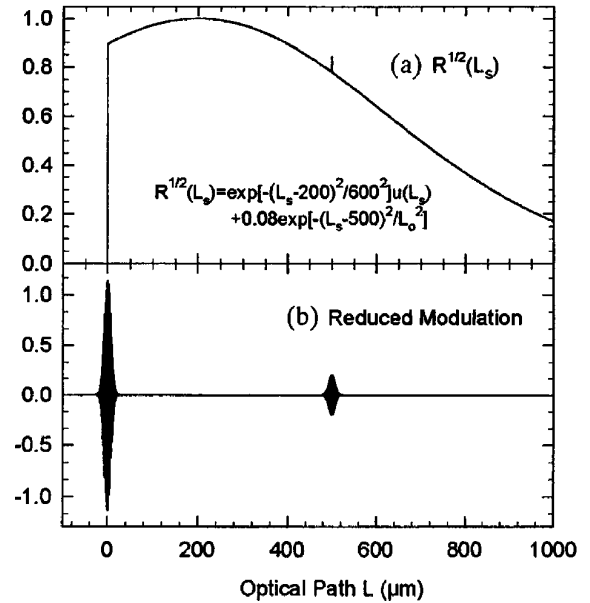which attenuates rapidly with the broadness L_0 of the

Fig. 5. Calculated path-length-resolved reflectance $R^{1/2}(L_s)$ and OCT modulation: (a) $R^{1/2}(L_s)$ is simulated as a sum of two Gaussians [$L_0 = 0.3$ μm, and $u(L_s)$ represents a step function]. (b) The interference modulation is calculated with Eq. (10) and plotted in arbitrary units.

Gaussian profile and saturates to $\exp(-4\bar{k}^2 L_0{}^2) \to 0$ when $L_0 > \lambda$. The first modulation peak in Fig. 5(b) is caused by the step rise of $R^{1/2}(L_s)$ at the surface $(L_s = 0)$, and at all other points from within the scattering medium where even $R^{1/2}(L_s)$ is much higher than the small perturbance when no modulation is induced. On the other hand, this result can be verified by a simple experiment that detects the modulation intensity from the first interface of a glass plate $(n_g = 1.56)$ that is immersed in a highly scattering liquid $(\mu_s = 50 \text{ cm}^{-1}, \mu_a = 0.1 \text{ cm}^{-1}, g = 0.8, n = 1.37)$. Figure 6(b) shows that no modulation peak, except at the surface and the glass interface, is readily detected from within the scattering medium.

From the above analysis we can conclude that although OCT is sometimes analogously considered as coherence-gated reflectometry, it is apparently different from time-resolved spectroscopy, because the time-resolved technique collects directly the reflected optical intensity within the time gate, whereas OCT traces out the local variations of the path-length-resolved reflectance. Therefore this phenomenon may be of extreme significance because it may provide a potential measure that extends the optical diagnosis to the microscopic extent, even though the algorithm for CT reconstruction is possibly complex.

3. Monte Carlo Simulation of Path-Length-Resolved Light Transport

To analyze quantitatively the relation of OCT modulation with tissue optical properties such as absorption coefficient μ_a, scattering coefficient μ_s, scattering

Fig. 6. Calculated $R(L_s)$ and measured OCT modulation of a glass slide $(n_g = 1.56)$ immersed $d_1 = 1.2$ mm deep in an Intralipid liquid $(\mu_s = 50 \text{ cm}^{-1}, \mu_a = 0.08 \text{ cm}^{-1}, g = 0.8, n_s = 1.37)$. R_{sp} is the specular reflectance at the air–Intralipid surface.

anisotropy g, and tissue optical inhomogeneity, the MC technique is applied to model the optical path-length-resolved diffuse reflectance from scattering media. The MC technique used here is modified from the general algorithm for time-resolved MC simulation that has been developed to offer solutions to the time-dependent radiative transfer equation. Although time-resolved diffusion approximation has led to explicit analytical expressions,[6] it is applicable only several picoseconds after an impulse corresponding to a few hundred micrometers' delay in the optical path-length domain between the signal and the reference arms of OCT. The MC method is, in principle, well suited for this case, despite the long calculation time. In this paper, we are concerned mainly with the longitudinal characteristics of OCT. Therefore, for simplicity in mathematics and suitability to describing the transition from specular to diffuse reflections, multilayer tissue phantoms are assumed.

The principle of MC simulation, which has been outlined elsewhere,[32] is to trace the photon's migration history and to calculate the light distribution within the tissue as well as the photon's escaping from the boundary after an impulse of irradiance with infinitely small beam diameter and narrow pulse duration [for a one-dimensional (1-D) tissue model]. Because of the radial symmetry of the light source and tissue optical properties in different tissue layers, the simulation can be implemented on a cylindrical model to minimize the dimensionality of reflectance calculation to three variables (r, θ, L) and to accelerate the calculation. r, θ, L refer to radial position, inclination with the incident beam, and the path length, respectively. The variable step method is also used to accelerate the calculation.

Each photon with an initial weight of unity $(w = 1)$ and zero path length $(L = 0)$ is launched normal to the tissue surface. A small fraction R_{sp} is discounted from w accumulated as specular reflectance at the surface, and the rest, $w = 1 - R_{sp}$, proceeds to migrate through the tissue in variable steps of free path between each successive interaction site, which can be given by

$$\Delta L = -\ln(\xi)/\mu_t, \qquad (13)$$

where $\mu_t = \mu_a + \mu_s$ is the total attenuation coefficient that is a reciprocal of the mean-free-path, and $0 < \xi < 1$ is a uniformly distributed pseudorandom number produced by a computer. At each interaction site, a fraction of the photon's weight is deposited because of absorption $w \leftarrow (\mu_s/\mu_t)w$, and then the photon's trajectory is deflected into a new direction according to a scattering function $p(\theta)$ that is defined by the Henyey–Greenstein function as an approximation of Mie scattering. If the photon strikes the boundary of the multilayer tissue, reflection or refraction can be determined by Fresnel's law specified in statistical form. When refracted into another layer, the photon state of migration is refreshed at the
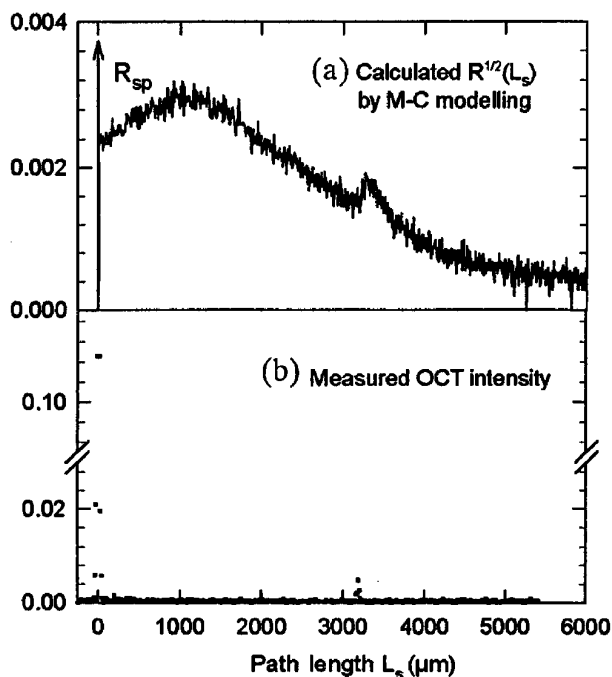
interface:

$$n_{i+1} \cos \theta_{i+1}^{x(y)} = n_i \cos \theta_i^{x(y)},$$

$$n_{i+1} \cos \theta_{i+1}^{z} = n_i \cos \theta_i^{z},$$

$$\Delta L_{i+1} = (\Delta L - \Delta L_i)\mu_t^i/\mu_t^{i+1}, \qquad (14)$$

where n_i and μ_t^i are the refractive index and the scattering coefficient of the ith layer, respectively. The path length is accumulated after each free path: $L \leftarrow L + n_i\Delta l$. By the repetition of the above procedures, the rays are traced until the photon is terminated in the following cases: either w is too small to take into account as a result of tissue absorption, L is longer than the path-length range of interest, or surface losses that are due to escape from tissue accumulate as path-length-resolved reflectance:

$$R(i, j, k) = R(i, j, k) + w, \qquad (15)$$

where i $(i = r/\Delta r)$, $j(i = \phi/\Delta\phi)$, and k $(k = L/\Delta L)$ are radial, angular, and temporal elements of the reflectance array, respectively. After all N $(N > 10^6)$ photons have been launched, $R(i, j, k)$ are converted to 1-D path-length-resolved reflectance arrays $R(L)$, depending on the geometry $(0 \sim r_0, 0 \sim \phi_0)$ of the detecting optics, as shown in Fig. 3:

$$R(r \leq r_0, \phi \leq \phi_0, L) = \frac{1}{N} \sum_{i \leq i_0} \sum_{j \leq j_0} \frac{1}{\Delta L} R(i, j, k). \quad (16)$$

The simulation is performed on a PC-486 personal computer with a 66-MHz main frequency and 32-Mbyte expanded memory specification for the allocation of array $R(i, j, k)$. Even so, the calculation is substantially time-consuming and usually requires at least 20 h. As OCT is extremely sensitive to the relative variations of $R^{1/2}(L)$, the path-length range close to the interface is zoomed in with variable grids even as narrow as 0.1 μm to offer the required database for the numerical convolution by Eq. (9). In addition, different spatial and temporal filters are inserted during the calculation of Eq. (16) in order to simulate the corresponding optical configurations, such as confocal system, etc.

4. Results and Analyses

The experiments are made on a conventional bulk-type Michelson interferometer similar to that depicted in Fig. 1. A commercially available laser diode (EG&G-TOLD9211) biased below lasing threshold is employed as the low-coherence light source. The central wavelength $\bar{\lambda}$ of the light source is 0.67 μm, and the coherent length L_c, measured by the use of the experimental setup, is 16 μm. The light beam is collimated to illuminate the Michelson interferometer in which both the reference mirror and the probe are mounted on translation stages driven by computer-controlled stepper motors. These two beams are recombined at detector PD, then preamplified and fed to a personal computer by a 16-bit analog–digital

(A/D) converter. The envelope of the interferogram can be demodulated by means of optical heterodyne detection that locks in the Doppler frequency $f_d = 2v_r/\bar{\lambda}$, which refers to the line speed v_r of piezoelectric transducer movement.

Figure 7 shows the relation of OCT modulation with the mean wavelength $\bar{\lambda}$ calculated with Eq. (10). The modulation amplitude is found to increase with $\bar{\lambda}$. This is because the higher the ratio $\bar{\lambda}/L_c$, the less the destructive interference will affect the low-coherence correlation, which is in fact filtering out the fast-varying components with $k \approx \bar{k}$ according to Fig. 4. On the other hand, the scattering coefficient μ_s in most tissues decreases with wavelength λ, leading to a deeper diffusion range for light penetration. Consequently an OCT system that employs a longer wavelength SLD, such as $\bar{\lambda} \approx 1.3$–1.5 μm, is preferable for turbid tissue measurements.

A. Results of Monte Carlo Simulation for $R_d(L_s)$ and the Calculated Optical Low-Coherence Tomography Response

Figures 8–12 summarize the results of MC modeling for the path-length-resolved diffuse reflectance from several typical tissue optical structures. As proposed in Section 2, OCT responds to the variations of path-length-resolved reflectance $R_d^{1/2}(L)$. In most cases below, the samples are assumed to be two-layer tissue phantoms; therefore the calculated curves may provide straightforward relations that can be used to predict what OCT detects because of the changes of tissue-optical properties. Specular reflection at the air–tissue surface is neglected here.

Figure 8 shows the dependence of $R^{1/2}(L)$ on μ_{s2}, the scattering coefficient of the lower layer. $R^{1/2}(L)$ jumps at the interface of $L_1 = 2n_1d_1 = 1.37$ mm, and the peak magnitude increases with μ_{s2}. The inset in Fig. (8) shows the relation of interference modulation to μ_{s2} calculated with Eq. (9) and normalized with that of $\mu_{s2} = 480$ cm^{-1}. It can be easily seen that the increasing gradients in the low $\mu_{s2}(\mu_{s2} < 120$ cm$^{-1})$ region are higher than those in the high μ_{s2} region.
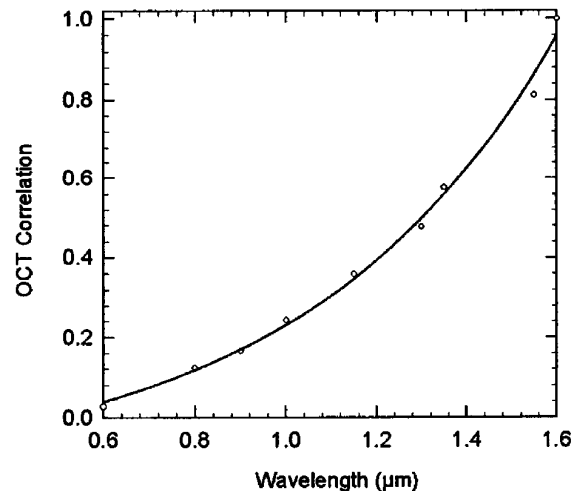

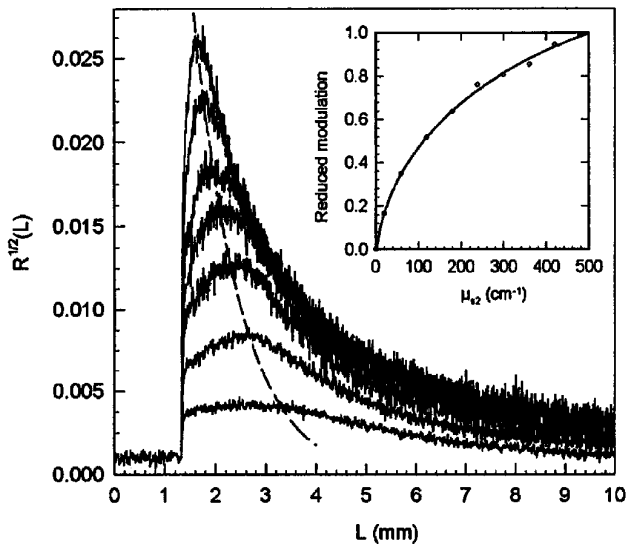Fig. 7. Relation of calculated OCT modulation with the mean wavelength $\bar{\lambda}$ of light.

Fig. 8. Path-length-resolved diffuse reflectance $R^{1/2}(L)$ for different μ_{s2} of the lower layer: $\mu_{a1} = \mu_{a2} = 0.1$ cm^{-1}, $g_1 = g_2 = 0.83$, $n_1 = n_2 = 1.37$, $d_1 = 0.05$ cm, $d_2 = 0.05$–2 cm, $\mu_{s1} = 3$ cm^{-1}, $\mu_{s2} = 20$, 60, 120, 180, 240, 360, 480 cm^{-1}. The dashed curve is fit by an exponential function.

Fig. 10. Path-length-resolved diffuse reflectance $R^{1/2}(L)$ from semi-infinite phantoms with different scattering anisotropy g: $\mu_a = 1$ cm^{-1}, $\mu_s = 100$ cm^{-1}, $n = 1.37$, $g = 0$, 0.3, 0.6, 0.8. Specular reflectance at the air–phantom surface is neglected.

This can be explained by the fact that, as $\mu_{s1} \ll \mu_{s2}$, the photon diffusion is predominated by the reduced scattering coefficient of the second layer, i.e., $\mu_{s2}' = \mu_{s2} (1 - g)$. When μ_{s2} increases, the diffusion range moves toward the interface, as indicated by the dashed curve, so more diffusely reflected light near the interface will be included in $R^{1/2}(L)$, whose path length is just a little longer than that of the least-backscattered photons. Quantitative analysis reveals that at the interface all the curves jump initially with nearly the same gradient that corresponds to the least-backscattered light from the interface, and then the gradients decline gradually with μ_{s2} resulting
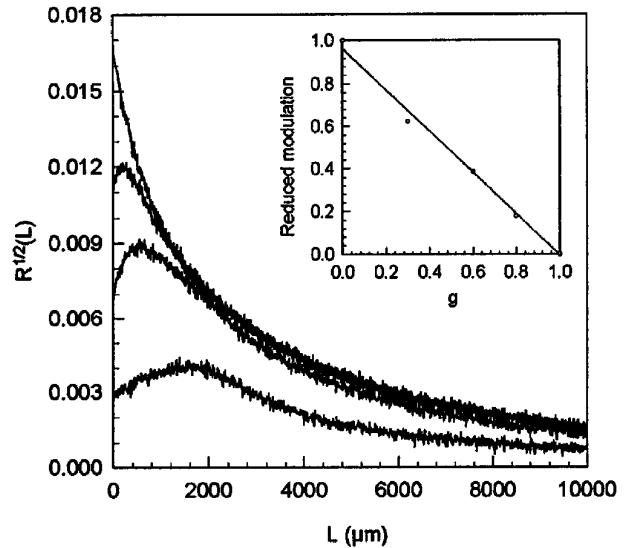
from the contributions of multiply scattered light. Further MC calculation reveals that the interference modulation decreases with d_1 because of multiple-scattering effects in the first layer. These effects imply that OCT responds primarily to the least-backscattered light.

Figure 9 shows the influence of absorption of the lower layer. As $\mu_{s1} \ll \mu_{s2}$ and $g > 0.8$, photon diffusion occurs mainly in the second layer. According to the time-dependent diffusion theory, the asymptotic slope of $R^{1/2}(L)$ versus pathlength L is exponentially proportional to the absorption coefficient μ_{a2}; however, the curves in the figure indicate that the magnitudes of maximum $R^{1/2}(L)$ at the interface are principally dependent on the reduced scattering coef-
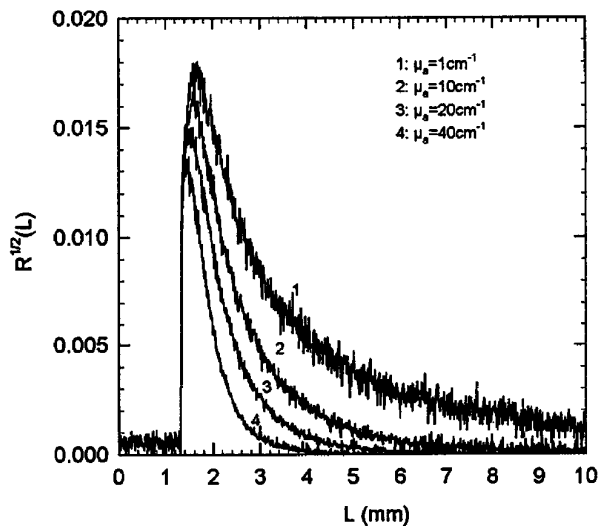

Fig. 9. Path-length-resolved diffuse reflectance $R^{1/2}(L)$ for different μ_{a2} of the lower layer: $\mu_{s1} = 1$ cm^{-1}, $\mu_{s2} = 100$ cm^{-1}, $g_1 = g_2 = 0.83$, $n_1 = n_2 = 1.37$, $d_1 = 0$–0.05 cm, $d_2 = 0.05$–2 cm, $\mu_{a1} = 1$ cm^{-1}, $\mu_{a2} = 1$, 10, 20, 40 cm^{-1}.
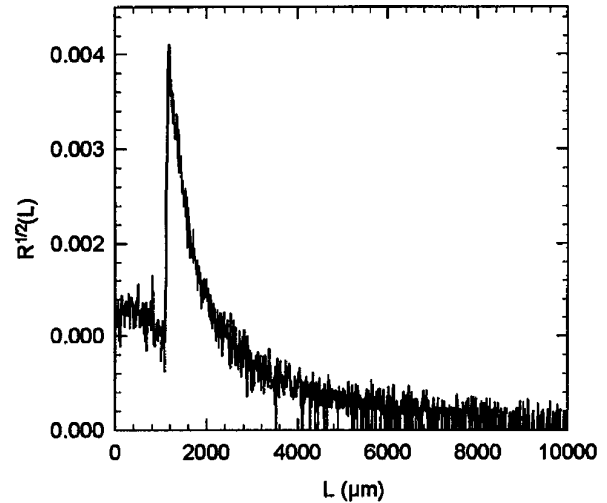

Fig. 11. Path-length-resolved diffuse reflectance $R^{1/2}(L)$ for a two-layer phantom with decreased scattering anisotropy g_2 in the lower layer: $\mu_{s1} = \mu_{s2} = 100$ cm^{-1}, $n_1 = n_2 = 1.37$, $d_1 = 0$–0.05 cm, $d_2 = 0.05$–2 cm, $\mu_{a1} = \mu_{a2} = 1$ cm^{-1}, $g_1 = 0.9$, $g_2 = 0.7$.
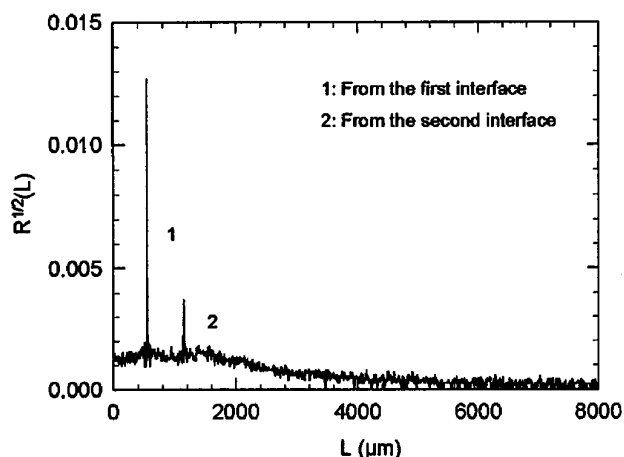
Fig. 12. Path-length-resolved diffuse reflectance $R^{1/2}(L)$ from a three-layer phantom with refractive-index mismatch: $\mu_{s1} = \mu_{s2} = \mu_{s3} = 100\ cm^{-1}$, $\mu_{a1} = \mu_{a2} = \mu_{a3} = 1\ cm^{-1}$, $g_1 = g_2 = g_3 = 0.83$, $n_1 = n_3 = 1.37$, $n_2 = 1.47$, $d_1 = d_2 = 0.02\ cm$, $L_1 = 2n_1 d_1 \approx 550\ \mu m$, $L_2 = 2(n_1 d_1 + n_2 d_2) \approx 1140\ \mu m$.

ficient μ_{s2}' and less affected by μ_{a2}. Thereafter, OCT is less sensitive to tissue absorption because $\mu_a \ll \mu_s'$ ($\mu_a < 5\ cm^{-1}$ in most tissues), which yields a steep rise of $R^{1/2}(L)$ compared with the relatively flat descending slope that is due to absorption [proportional to $\exp(-\mu_a L/2)$]. Nevertheless, the absorption can also influence the rising slope of $R^{1/2}(L)$. For example, increasing μ_{a1} gives rise to a higher modulation amplitude at the interface (as may be seen below in Fig. 15). In this case, the light that travels through longer scattering paths has a higher probability of being cut off by absorption, and therefore the absorptive thin layer on the top behaves like a low-path-length-pass filter that removes the multiply scattered light.

The calculated $R^{1/2}(L)$ for semi-infinite phantoms that have equal scattering and absorption coefficients ($\mu_a = 1\ cm^{-1}$, $\mu_s = 100\ cm^{-1}$) but that contain different sizes and shapes of scattering particles, i.e., different scattering anisotropies, are presented in Fig. 10. The inset demonstrates that the calculated modulation decreases linearly with g. This is due to the fact that, unlike scattering and absorption, which are path-accumulative procedures in which light attenuation occurs continuously along the scattering paths, a decrease in g causes a net increment of $R^{1/2}(L)$ at the interface, which will certainly induce a higher modulation similar to specular reflection. We extend our calculation to the case of a multilayer. Figure 11 shows the spike of the $R^{1/2}(L)$ curve at the interface $L_1 = 2n_1 d_1 = 1.37$ mm, demonstrating that even a slight decrease of g_2 from 0.9 to 0.7 causes a steep rise in $R^{1/2}(L)$, which will certainly induce higher interference modulation. Within the framework of current tissue optics, biological tissue is simply characterized by forward scattering, and the inhomogeneities in scattering anisotropy g are usually ignored, possibly because of difficulties for *in vivo* and *in vitro* measurements. Histological pictures reveal, however, that most tissues, such as skin, muscle, breast, and coronary arteries, consist of fibrous segments that may induce form birefringence and local scattering anisotropy. Therefore this result explains why a polarization-sensitive OCT is capable of identifying more microstructures in biological samples.

Figure 12 shows the $R^{1/2}(L)$ curve from a three-layer sample with only 7% of refractive-index mismatch at the second and the third interfaces ($n_1 = n_3 = 1.37$, $n_2 = 1.47$). Because each sharp spike corresponds to Fresnel's reflection, which is mathematically a pseudo-Dirac function $\delta(L - L_i)$, a grid resolution for temporal profile ΔL as narrow as 0.2 μm is adapted at the interfaces $L_i (i = 1, 2)$ in order to minimize the calculation error. Although the absolute reflection at the interface may be even lower than that induced by scattering, e.g., as shown in Fig. 8, as OCT responds to the relative variation of $R^{1/2}(L)$, a tiny change in refractive index ($\Delta n \approx 0.1$) can yield a substantial interference modulation that may be 10^3 times higher. Up to now, the refractive index of tissue is usually assumed to be 1.37 because of predominant water concentration; however, because of microstructural inhomogeneity and anisotropy in tissue, the local index of refraction $n(\mathbf{r})$ actually varies among different textured segments. It can therefore never be simply characterized by scattering effects for the ultrasensitive techniques that are capable of distinguishing micrometer-scale local structural difference. Unfortunately, nearly no research has been reported in this respect; nevertheless, based on the above analysis, OCT may become a promising method for microranging and localizing of biological tissues by detecting the local relative variations of the path-length-resolved backscattering.

B. Initial Experiments on Tissue Phantoms

To verify the theoretical prediction we have made for OCT in turbid media and the calculated results of MC modeling, we have performed some experiments. Figure 13 shows the calculated backscattered power curves plotted against the optical paths L that correspond to the depths of the mirror scanning longitudinally within the scattering phantom. In this experiment, a small mirror is inserted into a 40 mm × 40 mm × 25 mm glass cuvette filled with scattering liquid, i.e., 10% Intralipid dilution (Intralipid 10 Novum, $\mu_s = 50\ cm^{-1}$). A 5 mm × 5 mm hole is opened, and a 0.5-mm-thick objective glass plate is glued in as an optical window. The light beam from the SLD is collimated (to ~ϕ2 mm) to illuminate the probe. A 40-mm focal-length achromatic lens focused on the glass–Intralipid interface is used to collect the reflected light escaping from the scattering medium. A variable pinhole (adjusted to ~ϕ0.8–2 mm in the experiment) is inserted behind the beam splitter in which the signal and the reference beams converge, providing a collecting solid angle of 0.1–50 mrad to minimize the destructive interference at the detector that is due to the limited spatial coher-
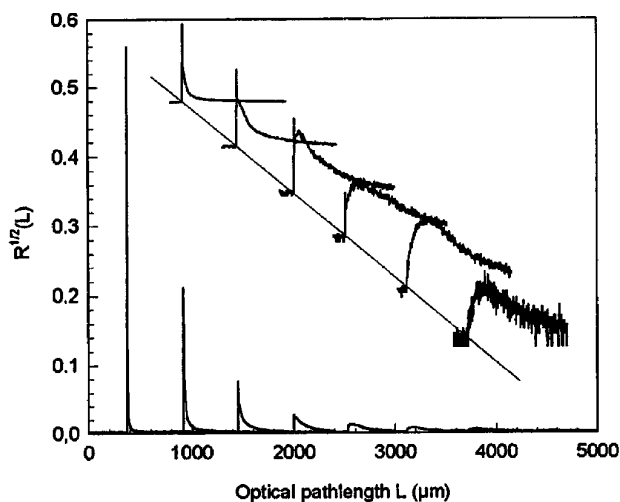
Fig. 13. Path-length-resolved reflectance $R^{1/2}(L)$ from a mirror scanning longitudinally within the scattering liquid: $\mu_s = 50$ cm^{-1}, $\mu_a = 0.1$ cm^{-1}, $g = 0.84$, $n = 1.33$.
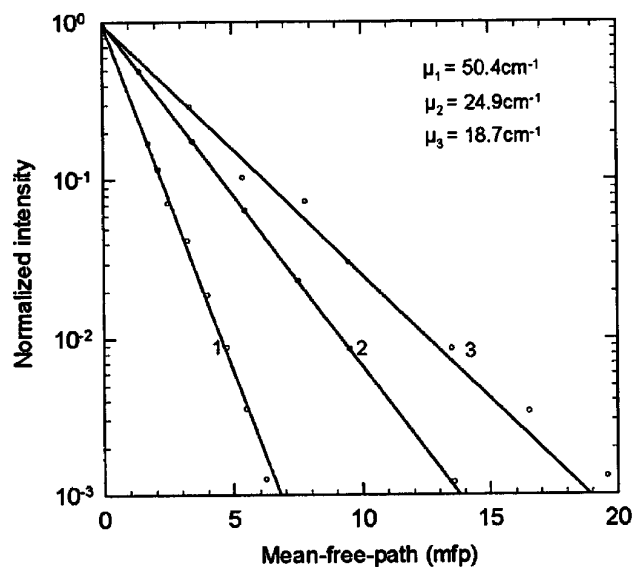

Fig. 14. Normalized backreflected intensity from a mirror versus the mfp of light transport in the scattering medium: 1, narrow-beam transmittance; 2, calculated OCT interference; 3, measured interference signal.

ence of the light source and the possible phase distortion, between the two arms, induced by the lens system.

The heavier curves of Fig. 13 show the relative variations of the backscattered spike shape as a function of mirror position $(L_1 = 2n_1d_1)$. As shown in the first two curves, a sharp spike consisting predominantly of specular reflection from the mirror is followed by a trail that lags behind as accumulative contributions of multiply scattered light. With the increase of optical path L_1, i.e., when the mirror is scanned deeper into the scattering phantom, this sharp spike of specular reflection decreases because of losses of collimated transmittance induced by scattering, becomes less obvious over the background of diffuse reflectance, and gradually vanishes at the position where the pathlength L_1 is nearly 3.7 mm. Therefore this experiment can characterize the response of OCT to the transition between specular and diffuse reflections. As shown in Fig. 14, the solid lines are the experimental results of light intensity plotted against the mfp (mfp $= \mu_t^{-1} \approx \mu_s^{-1}$). Line 1 is obtained by the direct measurement of the narrow-beam backreflected intensity, which is, in fact, the unscattered, collimated transmittance specularly reflected by the mirror. Apparently, according to Beer's law, it decreases exponentially with d_1 [i.e., $I_1(d_1) \propto \exp(-2\mu_t d_1)$] and the measured μ_t ($\mu_t = 49.4$ cm^{-1}) is in good agreement with the results of pinhole transmittance measurements reported elsewhere.[33] Line 2 is the calculated OCT modulation obtained with Eq. (9). As OCT employs optical heterodyne detection, which greatly enhances the interference modulation by multiplying $I_r^{1/2}$, the relation of the measured intensity with the distance can be expressed as

$$I_2(d_1) \propto \exp(-\mu_b 2d_1), \qquad (17)$$

where $\mu_b = \mu_t/2$. Note that $2d_1$ is the round-trip

geometric length from the surface to the mirror; therefore the attenuation ratio of I_2 versus d_1 is equal to that of the incoherent transillumination technique. Line 3 of Fig. 14 is the measured OCT modulation. A least-squares fit shows that it also decreases exponentially with d_1 [i.e., $I_3(d_1) \propto \exp(-\mu_3 2d_1)$]; however, the measured attenuation coefficient μ_3 ($\mu_3 = 18.8$ cm^{-1}) is smaller than the theoretical result ($\mu_c = 24.5$ cm^{-1}). There are several reasons that may cause such a deviation. For example, the experimental complication induced by confocal interference effects may give rise to an on-axis intensity modulation near the focal range. Hee et al.[34] once reported similar observations for forearm measurements. Further detailed analysis about this effect is worthwhile to do. From line 3 of Fig. 14 we can find that, although the noise reduction electronics of the initial experimental system is far from being optimized (less than 60-dB dynamic range), it can readily distinguish samples that are immersed 21 mfp deep into the scattering medium. So with the increase of optical power and improvement of signal processing electronics, a maximum detectable thickness up to 25–30 mfp should be attainable. On the other hand, if the coherence gate is kept constant, i.e., $L = 2n_1d_1$ and the probe is scanned laterally, coherence-gated transillumination can be easily achieved with this simple experimental setup. It can find practical applications for the *in vitro* measurements of biological tissues simply by the insertion of the sample in front of the mirror. Further investigation for *in vitro* tissue measurements is underway.

How to detect an OCT signal induced by the changes of μ_s and μ_a and how to reject specular reflection at the interface has long been a major difficulty in the experimental design. To solve this problem, we prepared multilayer samples as follows: we added a
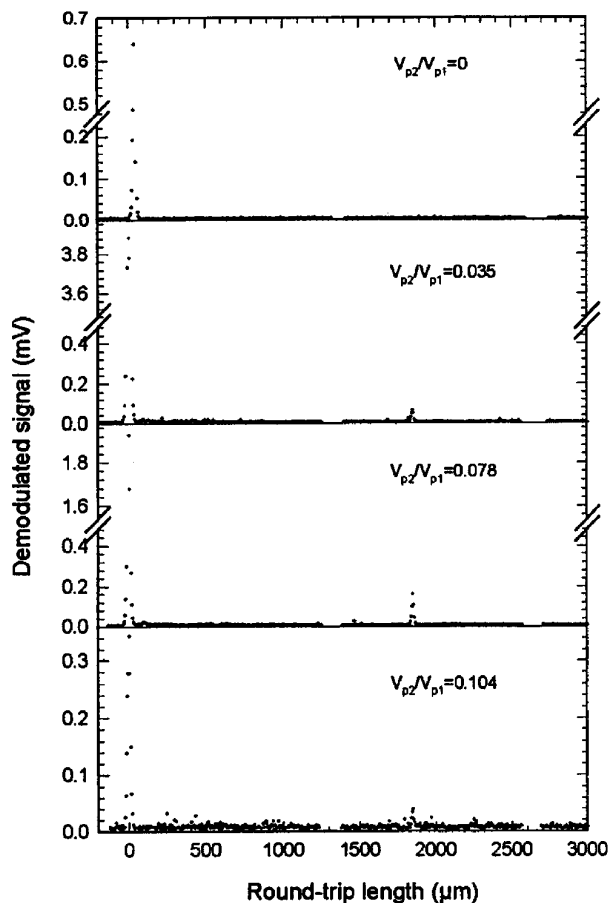
Fig. 15. Measured OCT modulation from two-layer scattering phantoms $(d_1 = 0.7\ \text{mm})$. Curve 1 in Fig. 16 shows that the specular reflection at the interface is successfully rejected. $R^{1/2}(L)$ that correspond to curves 1–4 are plotted in Fig. 16. V_{p1} and V_{p2} represent modulation amplitudes of specular reflectance at the surface and of backscattering at the interface that is due to increases of μ_{s2}, respectively.

The inset enlarges the transition range near the interface, which clearly shows that slightly increasing μ_{a1} and minimizing the aperture of the detecting optics increase the rising slope $dR^{1/2}(L)/dL$. This is because multiply scattered light has a longer path length and accordingly less probability of escaping from the scattering medium because of absorption and being collected by a pinhole detector because of diffusely reflected angular distribution. On the other hand, a quantitative comparison of the measured interference peaks in Fig. 15 shows that $(v_{p2}/v_{p1})_3 > (v_{p2}/v_{p1})_2 > (v_{p2}/v_{p1})_1$, where the amplitude at the interface v_{p2} is calibrated with that of the specular reflectance at the surface v_{p1} in order to remove the possible influence of other optical effects. This result also verifies our theoretical prediction that OCT responds to the relative variations of path-length-resolved backscattering.

5. Discussion

On the basis of white-light coherence theory and statistical optics, a theoretical model for OCT is presented that relates the modulation amplitude to path-length-resolved reflectance and that can be analyzed by means of a Fourier transform. Analysis of the model predicts that, unlike time-gated techniques, OCT measures the local relative variations of path-length-resolved reflectance; the path-length-resolved MC technique for multilayer tissues is implemented to simulate the possible variations of path-length-resolved backscattered light induced by local inhomogeneities of tissue-optical properties such as Δn, $\Delta\mu_s$, Δg, and $\Delta\mu_a$. The results show that OCT is very sensitive to Δn, then Δg and $\Delta\mu_s$, but insensitive to $\Delta\mu_a$, which implies that it may offer a promising method of detecting the local microstructural inhomogeneity and anisotropy. Initial experiments of a mirror scanning in a scattering medium that characterizes the transition from specular to diffuse reflec-

small portion (2% by volume concentration) of agar into the phantom liquid, heated the samples, and then heaped them sequentially during the solidification procedure. The mixture of Intralipid with agar will turn into a solid when the temperature decreases to $\sim$55 °C. Figure 15 shows the experimental curves of the normalized interference intensity versus path length for the two-layer samples. Except for curve 1, the scattering coefficients of the second layers are 480 cm^{-1}. To ensure that no mismatch of refractive index at the interface between these two layers is induced during the sample preparation, sample 1 is made following the same procedure given above but with the same phantom used for both layers, i.e., $\mu_{s1} = \mu_{s2} = 5\ \text{cm}^{-1}$. Curve 1 shows that no interference peak is detected at the interface $(L_1 \approx 1.7\ \text{mm})$; therefore the specular reflection is successfully rejected, and the small modulation peaks near $L_1 = 1.7$–1.8 mm in curves 2–4 apparently result from the difference of scattering coefficients at the interface. The path-length-resolved reflectances corresponding to these two-layer phantoms are plotted in Fig. 16.
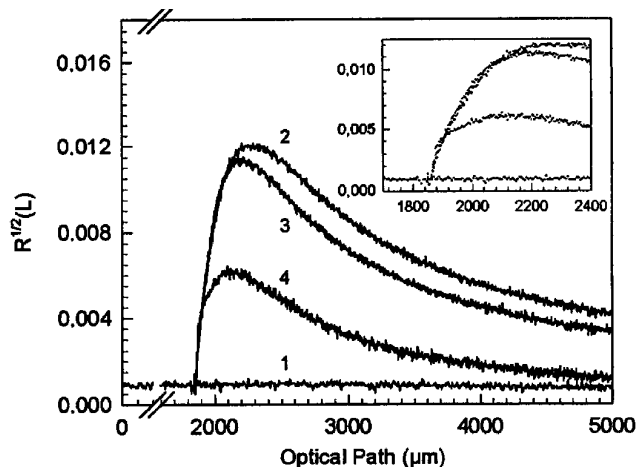

Fig. 16. Path-length-resolved reflectance from the interface of a two-layer scattering phantom: $g_1 = g_2 = 0.84$, $n_1 = n_2 = 1.33$, $\mu_{s1} = 6\ \text{cm}^{-1}$, $d_1 = 0.07\ \text{cm}$, $\mu_{a2} = 0.08\ \text{cm}^{-1}$. 1, $\mu_{s2} = \mu_{s1} = 6$ cm^{-1}; 2, $\mu_{s2} = 496\ \text{cm}^{-1}$, $\mu_{a1} = 0.08\ \text{cm}^{-1}$, broad beam; 3, $\mu_{s2} = 496$ cm^{-1}, $\mu_{a1} = 0.4\ \text{cm}^{-1}$, broad beam; 4, $\mu_{s2} = 496\ \text{cm}^{-1}$, $\mu_{a1} = 0.4$ cm^{-1}, narrow beam.

tions and for multilayer phantoms with differences in scattering coefficients are in agreement with the theoretical predictions.

It must be pointed out that, as multiply scattered light loses coherence, $R^{1/2}(L_s)$ should be reduced to the least-scattered light in the model calculation. As OCT responds primarily to the micrometer-range local relative variations of path-length-resolved backscattering, tissue can no longer be assumed to be a homogeneous medium characterized simply by scattering coefficient, as tissue has been treated so far, but should be considered as an optically heterogeneous composition of microstructural segments. Further experimental investigations concerning these speckle-related phenomena will be presented in a later publication.

References

1. C. H. Barlow, D. H. Burns, and J. B. Callis, "Breast biopsy analysis by spectroscopic imaging," in *Photon Migration in Tissues,* B. Chance ed. (Plenum, New York, 1989), pp. 111–119.
2. D. T. Delpy, M. Cope, P. van der Zee, S. Arridge, S. Wray, and J. Wyatt, "Estimation of optical pathlength through tissue from direct time of flight measurements," Phys. Med. Biol. **33,** 1422–1442 (1988).
3. B. Chance, K. Kang, and E. Sevick, "Photon diffusion in breast and brain: spectroscopy and imaging," Opt. Photon. News **4**(10), 9–13 (1993).
4. A. Rebane and J. Feinberg, "Timed-resolved holography," Nature **351,** 487–489 (1991).
5. D. A. Benaron and D. K. Stevenson, "Optical time-of-flight absorbance imaging of biomedical media," Science **259,** 1443–1446 (1993).
6. M. S. Patterson, B. Chance, and B. C. Wilson, "Time resolved reflectance and transmittance for the noninvasive measurement of tissue optical properties," Appl. Opt. **28,** 2331–2336 (1989).
7. B. Chance, J. S. Leigh, H. Miyake, D. S. Smith, S. Nioka, R. Greenfield, M. Finander, K. Kaufmann, W. Levy, M. Young, P. Cohen, H. Yoshioka, and H. Boretsky, "Comparison of time-resolved and unresolved measurements of deoxyhemoglobin in brain," Proc. Natl. Acad. Sci. USA **85,** 4971–4975 (1988).
8. F. Liu, K. M. Yoo, and R. R. Alfano, "Ultrafast laser-pulse transmission and imaging through biological tissues," Appl. Opt. **32,** 554–558 (1993).
9. R. Berg, O. Jarlman, and S. Svanberg, "Medical transillumination imaging using short-pulse diode lasers," Appl. Opt. **32,** 572–579 (1993).
10. G. Yoon, D. N. G. Roy, and R. C. Straight, "Coherent backscattering in biological media: measurement and estimation of optical properties," Appl. Opt. **32,** 580–584 (1993).
11. K. W. Berndt and J. R. Lakowicz, "Detection and localization of absorbers in scattering media using frequency-domain principles," in *Time-Resolved Spectroscopy and Imaging of Tissues,* B. Chance and A. Katzir, eds., Proc. Soc. Photo-Opt. Instrum. Eng. **1431,** 149–160 (1991).
12. J. Weng, M. Z. Zhang, K. Simons, and B. Chance, "Measurement of biological tissue metabolism using phase modulation spectroscopic technology," in *Time-Resolved Spectroscopy and Imaging of Tissues,* B. Chance and A. Katzir, eds., Proc. Soc. Photo-Opt. Instrum. Eng. **1431,** 161–170 (1991).
13. J. D. Briers, "Speckle fluctuations and biomedical optics: implications and applications," Opt. Eng. **32,** 277–283 (1993).
14. E. Leith, E. Arons, H. Chen, Y. Chen, D. Dilworth, J. Lopez, M. Shih, P.-C. Sun, and G. Vossler, "Electronic holography for imaging through tissue," Opt. Photon. News **4**(10), 19–23 (1993).
15. J. C. Hebden, "Line scan acquisition for time-resolved imaging through scattering media," Opt. Eng. **32,** 626–633 (1993).
16. Y. Yamada, Y. Hasegawa, and H. Maki, "Simulation of time-resolved optical computer tomography imaging," Opt. Eng. **32,** 634–641 (1993).
17. A. Knüttel, J. M. Schmitt, and J. R. Knuttson, "Spatial localization of absorbing bodies by interfering diffusive photon-density waves," Appl. Opt. **32,** 381–389 (1993).
18. M. Essenpreis, C. E. Elwell, M. Copy, P. van der Zee, S. R. Arridge, and D. T. Delpy, "Spectral dependence of temporal point spread functions in human tissues," Appl. Opt. **32,** 418–425 (1993).
19. L. Wang, P. P. Ho, and R. R. Alfano, "Time-resolved Fourier spectrum and imaging in highly scattering media," Appl. Opt. **32,** 5043–5049 (1993).
20. J. Reintjes, M. Bashkansky, M. D. Durcan, R. Mahon, L. L. Tankersley, J. A. Moon, C. L. Adler, and J. M. S. Prewitt, "Time-gated imaging with nonlinear optical Raman interactions," Opt. Photon. News **4**(10), 28–32 (1993).
21. G. S. Kino and S. S. C. Chim, "Mirau correlation microscope," Appl. Opt. **29,** 3775–3783 (1990).
22. T. Dresel, G. Häusler, and H. Venzke, "Three-dimensional sensing of rough surfaces by coherence radar," Appl. Opt. **31,** 919–925 (1992).
23. C. K. Hitzenberger, W. Drexler, and A. F. Fercher, "Measurement of corneal thickness by laser Doppler interferometry," Invest. Ophthalmol. Vis. Sci. **33,** 98–103 (1992).
24. D. Huang, E. A. Swanson, C. P. Lin, J. S. Schuman, W. G. Stinson, W. Chang, M. R. Hee, T. Flotte, K. Gregory, C. A. Puliafito, and J. G. Fujimoto, "Optical coherence tomography," Science **254,** 1178–1181 (1991).
25. E. A. Swanson, D. Huang, M. R. Hee, J. G. Fujimoto, C. P. Lin, and C. A. Puliafito, "High-speed optical coherence domain reflectometry," Opt. Lett. **17,** 151–153 (1992).
26. D. Huang, J. Wang, C. P. Lin, C. A. Puliafito, and J. G. Fujimoto, "Micro-resolution ranging of cornea anterior chamber by optical reflectometry," Lasers Surg. Med. **11,** 419–425 (1991).
27. M. R. Hee, J. A. Izatt, J. M. Jacobson, E. A. Swanson, and J. G. Fujimoto, "Time-gated imaging with femtosecond transillumination optical coherence tomography," in *Photon Migration and Imaging in Random Media and Tissues,* R. R. Alfano and B. Chance, eds., Proc. Soc. Photo-Opt. Instrum. Eng. **1888,** 28–37 (1993).
28. M. Born and E. Wolf, *Principles of Optics* (Pergamon, Oxford, 1970), Chap. X, pp. 491–554.
29. J. B. Develis, G. B. Parrent, G. O. Reynolds, and B. J. Thompson, eds., *The New Physical Optics Notebook: Tutorials in Fourier Optics,* Vol. PMO1 of SPIE Press Monograph Series (Society of Photo-Optical Instrumentation Engineers, Bellingham, Wash., 1989), Chaps. 18 and 23.
30. J. W. Goodman, *Statistical Optics* (Wiley, New York, 1984), Chap. 5.
31. C. F. Bohren and D. R. Huffman, *Absorption and Scattering of Light by Small Particles* (Wiley, New York, 1983), Chaps. 2, 4, and 5.
32. S. L. Jacques, "Time resolved propagation of ultrashort laser pulses within turbid tissues," Appl. Opt. **28,** 2223–2229 (1989).
33. Y. T. Pan, R. Engelhardt, J. Rosperich, G. Hüttmann, and R. Birngruber, "Measurement of optical-interaction-coefficient of Intralipid in visible and NIR range," in *Laser-Tissue Interaction V,* S. L. Jacques, ed., Proc. Soc. Photo-Opt. Instrum. Eng. **2134A,** 354–363 (1994).
34. M. R. Hee, D. Huang, E. A. Swanson, and J. G. Fujimoto, "Polarization-sensitive low-coherence reflectometer for birefringence characterization and ranging," J. Opt. Soc. Am. B **9,** 903–908 (1992).